Control of SMES systems in distribution networks with renewable energy integration: A perturbation estimation approach

Bo Yang [a], Junting Wang [a], Xiaoshun Zhang [b, *], Lei Yu [a], Hongchun Shu [a], Tao Yu [c], Liming Sun [d]

[a] Faculty of Electric Power Engineering, Kunming University of Science and Technology, 650500, Kunming, China
[b] College of Engineering, Shantou University, 515063, Shantou, China
[c] College of Electric Power, South China University of Technology, 510640, Guangzhou, China
[d] Guangzhou ShuimuQinghua Technology CO. LTD, 510898, Guangzhou, China

ABSTRACT

Electrical energy storage system (EESS) plays a crucial role to handle the intermittency and randomness of renewable energy, such that the power reliability can be significantly enhanced. This paper attempts to design an adaptive fractional-order sliding-mode control (AFOSMC) approach for a typical EESS technology, e.g., superconducting magnetic energy storage (SMES) systems, to improve its dynamical responses against varirous operation conditions. At first, a sliding-mode state and perturbation observer (SMSPO) is applied to estimate the combined effect of unmodelled dynamics, parameter uncertainties, and external disturbances of SMES systems. Then, a fractional-order sliding-mode control (FOSMC) is utilized to completely compensate the perturbation estimat, such that a noticeable robustness can be achieved. Moreover, only the dq-axis currents need to be measured while the perturbation estimate replaces its upper bound, thus AFOSMC be easily achieved with appropriate control costs. For the purpose of validating its control performance, a distribution network involving SMES system with renewable energy penetration is studied. The control performance of conventional proportional-integral-derivative (PID) control, interconnection and damping assignment passivity-based control (IDA-PBC), sliding-mode control (SMC), and fractional-order sliding-mode control (FOSMC) is compared to that of AFOSMC under three scenarios. Simulation results show that AFOSMC can greatly outperform other approaches in both tracking speed and overall costs, e.g., its active power error is only 63.55%, 83.44%, 69.60%, and 76.67% of that of PID control, IDA-PBC, SMC, and FOSMC under reactive and active power supply, while the required control costs is only 76.69%, 91.28%, 83.50, and 86.76% to the above three controllers. Finally, a hardware-in-the-loop (HIL) test based on dSpace is implemented to verify its practicability under various scenarios.

© 2020 Elsevier Ltd. All rights reserved.

1. Introduction

The development and utilization of renewable energy have become an urgent agenda for the sake of environment protection around the globe [1]. Generally speaking, the modern power system development has gradually evolved from smart grid to energy internet, and moving ahead to internet of things [2]. Under such paradigm, numerous applications of various renewable energy, i.e., wind, wave, solar, tidal, geothermal, hydro [3–5], have been popularly and widely investigated and applied worldwide [6].

However, large-scale penetration of renewable energy has caused plenty of severe problems, such as power balance, frequency modulation, and operation stability and security due to their inherent nature of randomness and intermittence [7,8].

Nowadays, electric energy storage systems (EESS) have played a crucial role in modern energy supply chain [9]. Such great significance of EESS thanks to their prominent merits of power system stability enhancement, auxiliary control of renewable energy, generation efficiency improvement, fossil energy conservation, as well as greenhouse gas emission reduction. There are an enormous variety of EESS while the main difference is the scale of time and size, which can be mainly categorized into energy-type storage system and power-type storage systems. The former mainly consists of pumped hydroelectric energy storage (PHES), fuel cell

Nomenclature

Variables

E_d	d-axis voltage of AC equivalent node
E_q	q-axis voltage of AC equivalent node
ω	electrical frequency of AC equivalent node
i_d	d-axis current flowing across the transformer
i_q	q-axis current flowing across the transformer
v_d	d-axis voltage at PWM-CSC terminal
v_q	q-axis voltage at PWM-CSC terminal
i_{dc}	DC current flowing across superconducting coil
m_d	d-axis modulation indicatrix
m_q	q-axis modulation indicatrix
P_{ac}	active power
Q_{ac}	reactive power

AFOSMC parameters

$\varsigma_i, \phi_i\ \lambda_{ci}\ (i=1,2)$	controller gains
$\alpha_{ij}, k_{ij}\ (i=1,2; j=1,2,3)$	observer gains
ε_o	the thickness layer boundary of the observer
ε_c	the thickness layer boundary of controller
$\alpha 1\ \alpha 2$	fractional differential order

SMES system parameters

C	capacitor used as low-pass filter
L_{sc}	inductance of superconducting coil device
L_T	inductance of transformer
R_T	resistance of transformer
S_{SMES}^{rated}	rated apparent power of SMES system

Abbreviations

SMES	superconductor magnetics energy storage
SMC	sliding-mode control
FOSMC	fractional-order SMC
AFOSMC	adaptive fractional-order SMC
PID	proportional-integral-derivative
SMSPO	sliding-mode state and perturbation observer
PWM-CSC	pulse-width modulated current source converter
HIL	hardware-in-the-loop
IDA-PBC	interconnection and damping assignment passivity-based control
IAE	integral of absolute error
EESS	electric energy storage systems
SCES	super-capacitor energy storage
FWES	super-capacitor energy storage
HESS	hybrid energy storage system
TES	thermal energy system
CAES	compressed air energy system
PHES	pumped hydroelectric energy storage
PCU	power converter unit
PCC	point of common coupling
PCH	port-controlled Hamiltonian
MPC	model predictive control
PO	perturbation observer
PERSFC	perturbation estimation based robust state feedback control
DFIG	doubly-fed induction generator
PoFoPID	perturbation observer based fractional-order PID

energy storage, as well as compressed air energy storage (CAES) and thermal energy storage (TES) with minimal environmental impact, while super-capacitor energy storage (SCES), superconducting magnetic energy storage (SMES), and flywheel energy storage (FWES) belong to the latter [10]. Moreover, hybrid energy storage system (HESS) composed of SCES and SMES could meet the needs of high storage capacity and rapid response [11].

Among aforementioned techniques, SMES systems have the merit of high conversion efficiency due to superconductors, e.g., low energy loss, low cost and high current-carrying capacity [12]. In addition, it is capable of rapidly and independently regulating active power/reactive power in four quadrants to effectively achieve power transfer control resulted from high-frequency power electronic switching devices [13]. A pulse-width modulated current source converter (PWM-CSC) has been widely used in SMES systems which can reduce the harmonic distortion and number of electronic components [14].

In SMES systems, the energy stored in magnet can be discharged via power converter unit (PCU) to power grid, such that a smooth and satisfactory power flow can be obtained at the point of common coupling (PCC). As a consequence, an important task of SMES systems operation is the design of proper controller for PCU. Conventional linear control scheme, e.g., proportional-integral-derivative (PID) control has been largely adopted because of its simple structure and high implementation reliability [15]. Nevertheless, SMES system is a nonlinear system with strong coupling, in which the control parameters of PID are selected through one-point linearization. Hence, PID control is not capable of providing a globally consistent control performance in different operations. To handle such thorny difficulty, many nonlinear control strategies have been developed. Lin, X.D [16]. proposed the port-controlled

Hamiltonian (PCH) models based energy-shaping mechanism of SMES systems to achieve a fast power commands response. Moreover, in order to improve dynamical responses under various operation conditions, a fuzzy logic control was employed for SMES system by Wang, S. [17]. Besides, Trilochan, P [18]. developed a nonlinear dynamic evolution control for SMES system, which can significantly suppress power harmonics. Moreover, for the sake of realizing a globally consistent control performance, Shi, J [19]. adopted a feedback linearization control to remove nonlinearities of SMES system. Meanwhile, an interconnection and damping assignment passivity-based control (IDA-PBC) was designed by Montoya, O.D. [20], which can enhance the transient response capability of SMES system. Furthermore, Wan, Y [21]. reported an extended backstepping control to improve the dynamic responses of SMES system. However, these approaches are mainly based on a full state measurement and precise system modelling, which therefore lacks of robustness to uncertainties in modelling. For the sake of improving the robustness, model predictive control (MPC) was devised which estimates uncertain parameters of SMES system [22]. Meanwhile, the robustness can be improved by sliding-mode control (SMC) [23].

Basically, SMES system often operates under various uncertainties resulted from stochastic feature of renewable energy while an optimal control performance is of great importance as the investment of SMES system is still quite high. However, the aforementioned nonlinear control strategies generally require a accurate SMES model, e.g., all/many states and parameters must be measured [16,19−21], which hinders their practical applications. Besides, the selection of proper fuzzy rule or evolution mechanism used in advanced approaches [17,18] remain to be unresolved. Meanwhile, other robust controllers normally result in over-

conservative control performance which inevitably causes unnecessary additional costs [22,23]. As a result, an adaptive controller which does not need accurate system model and only require few state and parameter measurement, as well as achieves more optimal control performance need to be developed for the practical and optimal SMES system applications.

For the sake of efficiently improving the robustness and dynamic responses of SMES system, a new adaptive fractional-order sliding-mode control (AFOSMC) strategy is proposed in this work, which incorporates perturbation observer (PO) gor robustness enhancement and fractional-order sliding-mode control (FOSMC) framework for dynamic response improvement. AFOSMC is a very powerful tool in handling various uncertainties which has been applied to photovoltaic inverters [24] and DC-DC converters used in HESS with electric vehicles [25]. The state-of-the-art contribution of this study can be outlined as follows:

- Compared with linear PID controller [15], the nonlinearities of SMES system are fully compensated by AFOSMC, such that a global consistent control performance can be achieved under various operation conditions;
- Compared with nonlinear controllers [16,19−21], no accurate SMES system model is required by AFOSMC. In particular, only dq-axis currents i_d and i_q need to be measured without any parameter information. Thus, AFOSMC is easy to be implemented in practice
- Compared with advanced controllers [17,18], AFOSMC employs a sliding-mode perturbation and state observer (SMPSO) [26−28] to estimate the aggregated effect of nonlinearities and various uncertainties in terms of a perturbation, which is completely compensated online. Hence, AFOSMC does not need any training/learning rules
- Compared with robust controllers [22,23], AFOSMC utilizes the real-time estimate of perturbation rather than its upper bound for the purpose of compensation. As a consequence, the inherent drawbacks of over-conservativeness of robust controllers can be effectively avoided, such that a more optimal control design can be achieved to reduce the investment costs of SMES system.

Lastly, the objective of this study is summarized by the following four aspects:

(a) *Globally consistent control*: AFOSMC aims to achieve a globally consistent control for SMES systems in the presence of significant time-varying operation condition due to stochastic renewable energy integration, such that AFOSMC installed SMES systems can operate more smoothly and consistently;

(b) *Robust control with reasonable costs*: AFOSMC attempts to enhance the robustness of SMES systems against various uncertainties, e.g., unknown parameters and unmodelled dynamics, via the use of SMSPO. Meanwhile, more resonable costs can be realized by real-time perturbation compensation, such that AFOSMC installed SMES systems can operate more reliably and economically;

(c) *Improved dynamical responses*: AFOSMC adopts fractional-order sliding-mode surface into the controller design to considerably improve the dynamical responses of SMES systems, such that AFOSMC installed SMES systems can rapidly respond to considerable operation condition variations;

(d) *Easy practical implementation*: AFOSMC merely requires the measurement of dq-axis currents without any other further information of SMES system states/parameters, such that

AFOSMC installed SMES systems can be easily implemented in practice.

2. SMES systems modelling

As schematically demonstrated in Fig. 1, SMES system is mainly composed of three parts: (a) Low-temperature/High-temperature superconducting (LTS/HTS) coil magnet; (b) Cryogenic refrigerator; and (c) Helium/Nitrogen liquid. A superconducting coil has been utilized in SMES system to connect power grid via a power modulation system [29,30]. It can be regarded as a constant current source that could store energy in a long period, as well as a backup device to input electric power into power grid in presence of external disturbances.

Fig. 2 illustrates three major configurations of SMES system [31], in which a PWM-CSC is preferable since superconducting coil owns an intrinsic current feature, i.e., energy can be stored by utilizing magnetic field [32]. Hence, PWM-CSC based SMES system will be studied in this paper. Besides, Kirchhoff's laws have been applied (see Fig. 3) in PWM-CSC's AC side to determine the active power [19].

Mathematical model of SMES systems connected with distribution networks is expressed as [20,32].

$$L_T \frac{d}{dt} i_d = -R_T i_d - \omega L_T i_q + v_d - E_d \tag{1}$$

$$L_T \frac{d}{dt} i_q = -R_T i_q + \omega L_T i_d + v_q - E_q \tag{2}$$

$$C \frac{d}{dt} v_d = -i_d - \omega C v_q + m_d i_{dc} \tag{3}$$

$$C \frac{d}{dt} v_q = -i_q + \omega C v_d + m_q i_{dc} \tag{4}$$

$$\frac{1}{2} L_{sc} \frac{d}{dt} i_{dc}^2 = -E_d i_d - E_q i_q \tag{5}$$

where each symbol can be referred to Nomenclature.

As shown in Eq. (5), it is worth noting that the dynamical behaviour of current i_{dc} can be approximated by ignoring commutation and transformer losses because such power losses are lower than 5% of the entire transfer power [20]. Basically, reactive power Q_{ac} and active power P_{ac} are calculated by
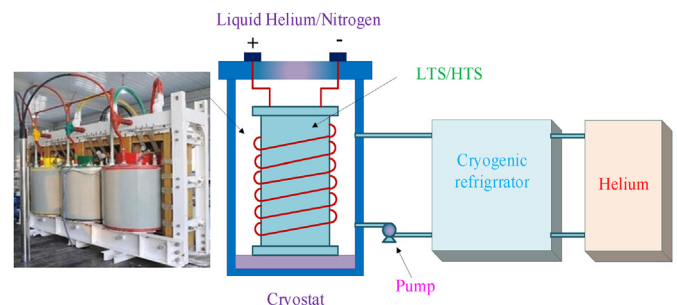
$$P_{ac} = E_d i_d + E_q i_q \tag{6}$$

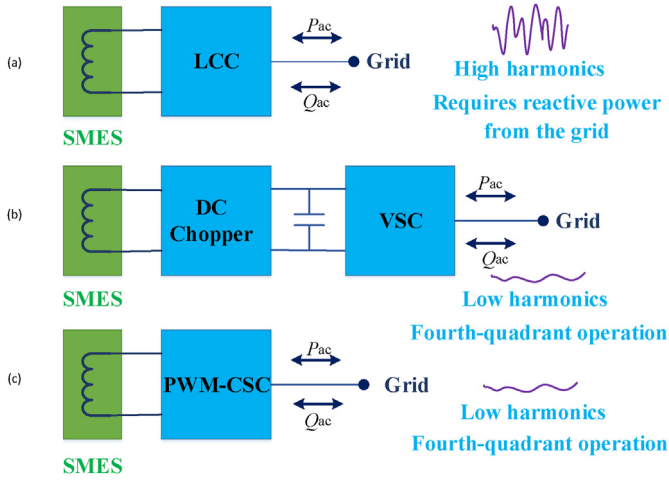**Fig. 1.** General components of SMES systems.

Fig. 2. Three typical structures of SMES system. (a) Line commutated converter (LCC), (b) Voltage source converter (VSC) and DC/DC converters, (c) Pulse-width-modulated current source converters (PWM-CSC).
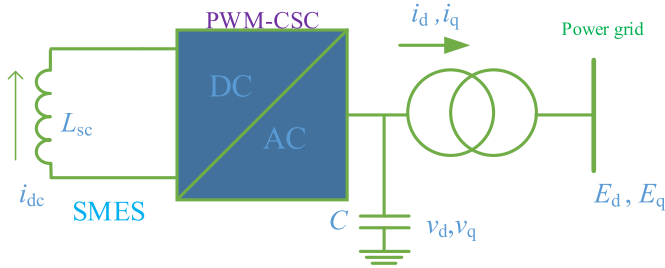

Fig. 3. Schematic diagram for SMES system based on PWM-CSC connected to AC power grid.

$$Q_{ac} = E_q i_d - E_d i_q \qquad (7)$$

3. Adaptive fractional-order sliding-mode control

3.1. SMSPO design

The standard form of uncertain nonlinear systems is described by

$$\begin{cases} \dot{x} = Ax + B(a(x) + b(x)u + d(t)) \\ y = x_1 \end{cases} \qquad (8)$$

where $x = [x_1, x_2, \cdots, x_n]^T \in \mathscr{R}^n$ denotes the state variable vector; $y \in \mathscr{R}$ and $u \in \mathscr{R}$ represent the output of system and control input, respectively; $a(x): \mathscr{R}^n \mapsto \mathscr{R}$ and $b(x): \mathscr{R}^n \mapsto \mathscr{R}$ denote several unknown smooth functions; and $d(t): \mathscr{R}^+ \mapsto \mathscr{R}$ means an external disturbance varies with time, respectively. Furthermore, state matrix A and control matrix B can be expressed as

$$A = \begin{bmatrix} 0 & 1 & 0\cdots0 \\ 0 & 0 & 1\cdots0 \\ \cdots & \cdots & \cdots\cdots\cdots \\ 0 & 0 & 0\cdots1 \\ 0 & 0 & 0\cdots0 \end{bmatrix}_{n\times n}, B = \begin{bmatrix} 0 \\ 0 \\ \vdots \\ 0 \\ 1 \end{bmatrix}_{n\times 1} \qquad (9)$$

The perturbation of system (8) can be described by [26–28].

$$\psi(x, u, t) = a(x) + (b(x) - b_0)u + d(t) \qquad (10)$$

where b_0 denotes a user-defined constant control gain.

Furthermore, the last state x_n in system (8) is written as

$$\dot{x}_n = a(x) + (b(x) - b_0)u + d(t) + b_0 u = \psi(x, u, t) \qquad (11)$$

Now, the perturbation can be represented via defining an extended state, e.g., $x_{n+1} = \psi(x, u, t)$. Hence, system (8) can be further expressed as

$$\begin{cases} y = x_1 \\ \dot{x}_1 = x_2 \\ \vdots \\ \dot{x}_n = x_{n+1} + b_0 u \\ \dot{x}_{n+1} = \dot{\psi}(\cdot) \end{cases} \qquad (12)$$

The new state vector can be represented as $x_e = [x_1, x_2, \cdots, x_n, x_{n+1}]^T$ and two assumptions are proposed as follows [26–28]:

A.1 b_0 must strictly satisfy the inequality $|b(x)/b_0 - 1| \leq \theta < 1$, in which θ represents a positive constant.

A.2 The perturbation $\psi(x, u, t): \mathscr{R}^n \times \mathscr{R} \times \mathscr{R}^+ \mapsto \mathscr{R}$ and its first-order derivative $\dot{\psi}(x, u, t): \mathscr{R}^n \times \mathscr{R} \times \mathscr{R}^+ \mapsto \mathscr{R}$ are limited as $|\psi(x, u, t)| \leq \gamma_1$, $|\dot{\psi}(x, u, t)| \leq \gamma_2$ with $\psi0, 0, 0 = 0$, and $\dot{\psi}0, 0, 0 = 0$, where positive constants γ_1 and γ_2 denote the limits of perturbation and its first-order derivative, respectively.

Denote $\tilde{x} = x - \hat{x}$ as the estimation error of x while $\hat{x}$ denotes the estimate of x, and $x*$ is the reference of x, respectively. Besides, the perturbation and states of extended system (10) can be estimated as follows [26–28]:

$$\begin{cases} \dot{\hat{x}}_1 = \hat{x}_2 + \alpha_1 \tilde{x}_1 + k_1 tanh(\tilde{x}_1, \varepsilon_o) \\ \vdots \\ \dot{\hat{x}}_n = \hat{\psi}(\cdot) + \alpha_n \tilde{x}_1 + k_n tanh(\tilde{x}_1, \varepsilon_o) + b_0 u \\ \dot{\hat{\psi}}(\cdot) = \alpha_{n+1} \tilde{x}_1 + k_{n+1} tanh(\tilde{x}_1, \varepsilon_o) \end{cases} \qquad (13)$$

where Luenberger observer gains $\alpha_i = C_{n+1}^i \lambda_\alpha^i, i = 1, 2, \cdots, n+1$, while sliding surface observer gains $k_i = C_n^i \lambda_k^i k_1, i = 1, 2, \cdots, n$.

Moreover, continuous and smooth $tanh(\tilde{x}_1, \varepsilon_o)$ function (ε_o represents the thickness layer bound of the observer) replaces discontinuous $sgn(\tilde{x}_1)$ function used in SMC, thus the effect of chattering can be considerably alleviated, as follows [33]:

$$tanh(x, \varepsilon) = \frac{e^{\frac{x}{\varepsilon}} - e^{-\frac{x}{\varepsilon}}}{e^{\frac{x}{\varepsilon}} + e^{-\frac{x}{\varepsilon}}} \qquad (14)$$

3.2. Fractional-order sliding-mode controller design

The basic operator $_aD_t^\alpha$ of fractional-order integral can be designed as [34].

$$_aD_t^\alpha = \begin{cases} \frac{d^\alpha}{dt^\alpha}, & \alpha > 0 \\ 1, & \alpha = 0 \\ \int_a^t (d\tau)^{-\alpha}, & \alpha < 0 \end{cases} \qquad (15)$$

where a and t represent the lower and upper boundaries while $\alpha \in \mathscr{R}$ denotes the operation order.

Besides, Riemann-Liouville (RL) definition is utilized with *Gamma* function $\Gamma(\cdot)$, yields

$$_a\mathrm{D}_t^\alpha f(t) = \frac{1}{\Gamma(n-\alpha)} \frac{\mathrm{d}^n}{\mathrm{d}t^n} \int_a^t \frac{f(\tau)}{(t-\tau)^{\alpha-n+1}} \mathrm{d}\tau \tag{16}$$

where n represents the first integer which is greater than or equal to α, e.g., $n-1 \le \alpha < n$.

The estimated fractional-order PD^α sliding surface for system (8) is described by

$$\widehat{S}_{\mathrm{FO}} = \sum_{i=1}^n \left[\rho_i\left(\widehat{x}_i - y_{\mathrm{d}}^{(i-1)}\right) + \mathrm{D}^\alpha\left(\widehat{x}_i - y_{\mathrm{d}}^{(i-1)}\right) \right] \tag{17}$$

where positive constant λ_c represents the gain of fractional-order PD^α sliding surface.

Besides, $\widehat{S}_{\mathrm{FO}}$ is set to be 0, yields

$$\mathrm{D}^\alpha\left(\widehat{x}_i - y_{\mathrm{d}}^{(i-1)}\right) = -\rho_i\left(\widehat{x}_i - y_{\mathrm{d}}^{(i-1)}\right) \tag{18}$$

According to Refs. [35], one has $C = -\rho_i$ and $|\arg(\mathrm{eig}(C))| = \pi$. When $0 < \alpha < 2$, $|\arg(\mathrm{eig}(C))| > \alpha\pi/2$ always satisfy. Hence, dynamics of fractional-order PD^α sliding surface (17) tends to be gradually stable.

3.3. Overall AFOSMC design

Therefore, AFOSMC for system (8) is described by

$$u = \frac{1}{b_0}\left[y_{\mathrm{d}}^{(n)} - \widehat{\psi}(\cdot) - \varsigma\widehat{S}_{\mathrm{FO}} - \phi\tanh(\widehat{S}_{\mathrm{FO}}, \varepsilon_c) \right] \tag{19}$$

where ς and ϕ represent the gains of sliding-mode control. Furthermore, ε_c represents the thickness layer bound of controller.

Remark 1. The bound of perturbation and its derivative described in assumption **A.2** can be verified as follows:

Firstly, the equivalent dynamics of perturbation estimation error is expressed as [28].

$$\begin{cases} \dot{\widetilde{x}}_2 = -\dfrac{k_2}{k_1}\widetilde{x}_2 + \widetilde{x}_3 \\[2mm] \dot{\widetilde{x}}_3 = -\dfrac{k_3}{k_1}\widetilde{x}_2 + \widetilde{x}_4 \\[1mm] \quad\vdots \\[1mm] \dot{\widetilde{x}}_n = -\dfrac{k_n}{k_1}\widetilde{x}_2 + \widetilde{x}_n \\[2mm] \dot{\widetilde{x}}_{n+1} = -\dfrac{k_{n+1}}{k_1}\widetilde{x}_2 + \dot{\psi}(\cdot) \end{cases} \tag{20}$$

Then, substitute control law (19) into perturbation (10), together with the last equation of system (20), one can obtain the perturbation and its derivative by

$$\psi = \frac{b_0}{b(x)}[a(x) + d(t)] + \frac{[b(x) - b_0]}{b(x)}[\widetilde{x}_{n+1} - \varsigma\widehat{S}_{\mathrm{FO}} - \phi tanh(\widehat{S}_{\mathrm{FO}}, \varepsilon_c)] \tag{21}$$

$$\begin{aligned} \dot{\psi} &= \dot{a}(x) + \dot{d}(t) + \dot{b}(x)u + \frac{[b(x) - b_0]}{b_0}\Bigg[\\ &\quad - \dot{\psi} - \varsigma\dot{\widehat{S}}_{\mathrm{FO}} - \phi\frac{\mathrm{d}}{\mathrm{d}t}tanh(\widehat{S}_{\mathrm{FO}}, \varepsilon_c) \Bigg] \\ &= \dot{a}(x) + \dot{d}(t) + \dot{b}(x)u \\ &\quad + \frac{[b(x) - b_0]}{b_0}\Bigg[-\frac{k_{n+1}}{k_1}\widetilde{x}_2 - \varsigma\dot{\widehat{S}}_{\mathrm{FO}} - \phi\frac{\mathrm{d}}{\mathrm{d}t}tanh(\widehat{S}_{\mathrm{FO}}, \varepsilon_c) \Bigg] \end{aligned} \tag{22}$$

Based on assumption **A.1**, yields

$$|\psi| \le \frac{1}{1-\theta}[|a(x)| + |d(t)|] + \frac{\theta}{1-\theta}[|\widetilde{x}_{n+1}| + \varsigma|\widehat{S}_{\mathrm{FO}}| + \phi] \tag{23}$$

$$\begin{aligned} |\dot{\psi}| &\le |\dot{a}(x)| + |\dot{d}(t)| + \dot{b}(x)|u| + \theta\Bigg[\\ &\quad \times |\dot{\widetilde{x}}_{n+1}| + \varsigma|\dot{\widehat{S}}_{\mathrm{FO}}| + \phi\left|\frac{\mathrm{d}}{\mathrm{d}t}tanh(\widehat{S}_{\mathrm{FO}}, \varepsilon_c)\right|\Bigg] \end{aligned} \tag{24}$$

Lastly, consider the perturbation is a smooth function, assumption **A.2** can be proved. Note that the system parameters and disturbances are then synthesized into the perturbation, which is estimated by SMSPO (13).

4. AFOSMC design for SMES systems

4.1. Character analysis of SMES system

The dynamics of DC current i_{dc} is controlled by the dynamical response of i_{d} and i_{q}. The energy storage variable is defined as $z(t) = L_{\mathrm{sc}}i_{\mathrm{dc}}$, gives

$$\begin{cases} z(t) = \sqrt{z_0^2 - 2L_{\mathrm{sc}}\displaystyle\int_0^t s(\tau)\mathrm{d}\tau} \\[3mm] s(\tau) = E_{\mathrm{d}}i_{\mathrm{d}} + E_{\mathrm{q}}i_{\mathrm{q}} \end{cases} \tag{25}$$

where z_0 represents the state of energy storage variable z at initial stage and $s(\tau)$ means the transferred active power between AC and DC side.

Fig. 4 demonstrates the behaviour of the stored energy in superconducting coil, in which there exists two important points, denoted by A and C. Particularly, the minimum and maximum admissible energy of SMES system can be represented by them. In general, SMES system operates between point A and point C, e.g., denoted by point B, which active power reference can either be positive or negative (denoted by P). Here, the references of reactive and active power are represented as P_{ac}^* and Q_{ac}^*, respectively. Based on Eq. (6) and Eq. (7), the references of dq-axis currents i_{d}^* and i_{q}^* are written as

$$i_{\mathrm{d}}^* = \left(\frac{L_{\mathrm{T}}}{E_{\mathrm{d}}^2 + E_{\mathrm{q}}^2}\right)(E_{\mathrm{d}}P_{\mathrm{ac}}^*\beta + E_{\mathrm{q}}Q_{\mathrm{ac}}^*) \tag{26}$$

$$i_{\mathrm{q}}^* = \left(\frac{L_{\mathrm{T}}}{E_{\mathrm{d}}^2 + E_{\mathrm{q}}^2}\right)(E_{\mathrm{d}}P_{\mathrm{ac}}^*\beta - E_{\mathrm{q}}Q_{\mathrm{ac}}^*) \tag{27}$$

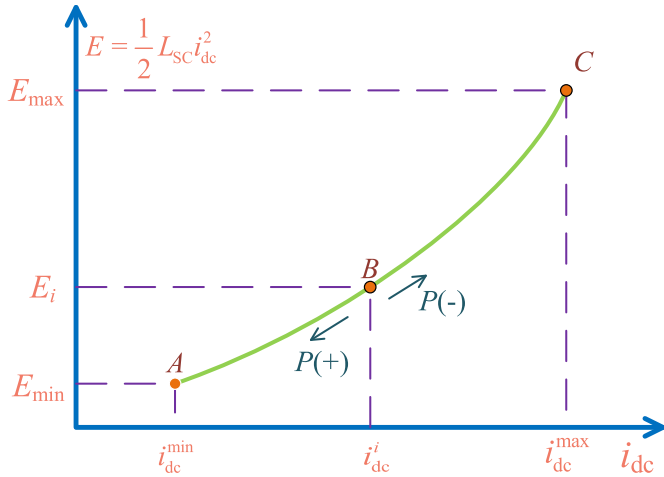where β represents the operation coefficient of SMES system which can be further written as

Fig. 4. Behaviour of the stored energy in the superconducting coil.

$$\beta = \begin{cases} 1, & z_{min} \le z \le z_{max} \\ 0, & otherwise \end{cases} \qquad (28)$$

4.2. Controller design

For SMES system (1)–(7), define state vector as $x = (x_1, x_2, x_3, x_4, x_5)^T = (i_d, i_q, v_d, v_q, i_{dc})^T$, output $y = (y_1, y_2)^T = (i_d, i_q)^T$, and control input $u = (u_1, u_2)^T = (m_d, m_q)^T$, respectively. Then, the state equation of SMES system (1)–(7) can be obtained as

$$\dot{x} = f(x) + g(x)u \qquad (29)$$

where

$$f(x) = \begin{pmatrix} f_1 \\ f_2 \\ f_3 \\ f_4 \\ f_5 \end{pmatrix} = \begin{pmatrix} -\dfrac{R_T}{L_T}x_1 - \omega x_2 + \dfrac{x_3}{L_T} - \dfrac{E_d}{L_T} \\[2mm] -\dfrac{R_T}{L_T}x_2 + \omega x_2 + \dfrac{x_4}{L_T} - \dfrac{E_q}{L_T} \\[2mm] -\dfrac{1}{C}x_1 - \omega x_4 \\[2mm] -\dfrac{1}{C}x_2 + \omega x_3 \\[2mm] \dfrac{-E_d x_1 - E_q x_2}{L_{sc}x_5} \end{pmatrix} \quad g(x) = \begin{pmatrix} 0 & 0 \\ 0 & 0 \\ \dfrac{x_5}{C} & 0 \\ 0 & \dfrac{x_5}{C} \\ 0 & 0 \end{pmatrix} \qquad (30)$$

Differentiate output y until control input u explicitly appeared, gives

Hence, system (31) is able to be concisely expressed in the form of matrix, as follows

$$\begin{bmatrix} \ddot{y}_1 \\ \ddot{y}_2 \end{bmatrix} = \begin{bmatrix} h_1(x) \\ h_2(x) \end{bmatrix} + B(x)\begin{bmatrix} u_1 \\ u_2 \end{bmatrix} \qquad (32)$$

where

$$h_1(x) = \left(\dfrac{R_T^2}{L_T^2} - \omega^2 - \dfrac{1}{CL_T}\right)i_d + \dfrac{2\omega R_T}{L_T}i_q + \dfrac{R_T}{L_T^2}(E_d - v_d) + \dfrac{w}{L_T}E_q - \dfrac{2w}{L_T}v_q - \dfrac{1}{L_T}\dot{E}_d \qquad (33)$$

$$h_2(x) = \left(\dfrac{R_T^2}{L_T^2} - \omega^2 - \dfrac{1}{CL_T}\right)i_q - \dfrac{2\omega R_T}{L_T}i_d + \dfrac{R_T}{L_T^2}(E_q - v_q) - \dfrac{w}{L_T}E_d + \dfrac{2w}{L_T}v_d - \dfrac{1}{L_T}\dot{E}_q \qquad (34)$$

with

$$B(x) = \begin{bmatrix} \dfrac{i_{dc}}{CL_T} & 0 \\[2mm] 0 & \dfrac{i_{dc}}{CL_T} \end{bmatrix} \qquad (35)$$

In particular, the control of dq-axis currents i_d and i_q is inherent coupled. Moreover, for the sake of guaranteeing the linearization of input-output introduced above to be effective, control gain matrix $B(x)$ requires to be nonsingular throughout all operation conditions, e.g.,

$$\det[B(x)] = \dfrac{i_{dc}^2}{C^2 L_T^2} \ne 0 \qquad (36)$$

As superconducting coil current i_{dc} is always different from zero ($i_{dc} \ne 0$ means that superconducting coil keeps operating, i.e., always under control), such that requirement (36) can always be guaranteed.

Define perturbations $\psi_1(\cdot)$ and $\psi_2(\cdot)$ for SMES system (32), gives

$$\begin{bmatrix} \psi_1(\cdot) \\ \psi_2(\cdot) \end{bmatrix} = \begin{bmatrix} h_1(x) \\ h_2(x) \end{bmatrix} + (B(x) - B_0)\begin{bmatrix} u_1 \\ u_2 \end{bmatrix} \qquad (37)$$

Furthermore, constant control gain matrix B_0 can be expressed as

$$B_0 = \begin{bmatrix} b_{11} & 0 \\ 0 & b_{22} \end{bmatrix} \qquad (38)$$

where b_{11} and b_{22} are the user-defined constant control gains.

$$\begin{cases} \ddot{y}_1 = \left(\dfrac{R_T^2}{L_T^2} - \omega^2 - \dfrac{1}{CL_T}\right)i_d + \dfrac{2\omega R_T}{L_T}i_q + \dfrac{R_T}{L_T^2}(E_d - v_d) + \dfrac{w}{L_T}E_q - \dfrac{2w}{L_T}v_q - \dfrac{1}{L_T}\dot{E}_d + \dfrac{1}{CL_T}i_{dc}m_d \\[3mm] \ddot{y}_2 = \left(\dfrac{R_T^2}{L_T^2} - \omega^2 - \dfrac{1}{CL_T}\right)i_q - \dfrac{2\omega R_T}{L_T}i_d + \dfrac{R_T}{L_T^2}(E_q - v_q) - \dfrac{w}{L_T}E_d + \dfrac{2w}{L_T}v_d - \dfrac{1}{L_T}\dot{E}_q + \dfrac{1}{CL_T}i_{dc}m_q \end{cases} \qquad (31)$$

Choose tracking error $e = [e_1, e_2]^T = [i_d - i_d^*, i_q - i_q^*]^T$, differentiate e until input u explicitly appear, gives

$$\begin{bmatrix} \ddot{e}_1 \\ \ddot{e}_2 \end{bmatrix} = \begin{bmatrix} \psi_1(\cdot) \\ \psi_2(\cdot) \end{bmatrix} + B_0 \begin{bmatrix} u_1 \\ u_2 \end{bmatrix} - \begin{bmatrix} \ddot{i}_q^* \\ \ddot{i}_d^* \end{bmatrix} \quad (39)$$

Define $z_{11} = i_d$, $z_{12} = \dot{z}_{11}$, then a third-order SMSPO is utilized by

$$\begin{cases} \dot{\hat{z}}_{11} = \hat{z}_{12} + \alpha_{11}\tilde{z}_{11} + k_{11}tanh(\tilde{z}_{11}, \varepsilon_o) \\ \dot{\hat{z}}_{12} = \hat{\psi}_1(\cdot) + \alpha_{12}\tilde{z}_{11} + k_{12}tanh(\tilde{z}_{11}, \varepsilon_o) + b_{11}u_1 \\ \dot{\hat{\psi}}_1(\cdot) = \alpha_{13}\tilde{z}_{11} + k_{13}tanh(\tilde{z}_{11}, \varepsilon_o) \end{cases} \quad (40)$$

where k_{11}, k_{12}, k_{13}, α_{11}, α_{12}, and α_{13} all represent positive observer gains.

Meanwhile, define $z_{21} = i_q$, $z_{22} = \dot{z}_{21}$, then a third-order SMSPO is utilized by

$$\begin{cases} \dot{\hat{z}}_{21} = \hat{z}_{22} + \alpha_{21}\tilde{z}_{21} + k_{21}tanh(\tilde{z}_{21}, \varepsilon_o) \\ \dot{\hat{z}}_{22} = \hat{\psi}_2(\cdot) + \alpha_{22}\tilde{z}_{21} + k_{22}tanh(\tilde{z}_{21}, \varepsilon_o) + b_{22}u_2 \\ \dot{\hat{\psi}}_2(\cdot) = \alpha_{23}\tilde{z}_{21} + k_{23}tanh(\tilde{z}_{21}, \varepsilon_o) \end{cases} \quad (41)$$

where observer gains k_{21}, k_{22}, k_{23}, α_{21}, α_{22}, and α_{23}, all denote positive observer gains.

The estimated fractional-order PD^α sliding surface of tracking error dynamics (39) is selected as

$$\begin{bmatrix} \hat{S}_{FO1} \\ \hat{S}_{FO2} \end{bmatrix} = \begin{bmatrix} D^{\alpha 1}(\hat{i}_d - i_d^*) + \lambda_{c1}(\hat{i}_d - i_d^*) \\ D^{\alpha 2}(\hat{i}_q - i_q^*) + \lambda_{c2}(\hat{i}_q - i_q^*) \end{bmatrix} \quad (42)$$

where $\alpha 1$ and $\alpha 2$ are the fractional differential orders, while λ_{c1} and λ_{c2} mean the gains of fractional-order PD^α sliding surface, respectively.

Lastly, AFOSMC law is given by

$$\begin{bmatrix} m_d \\ m_q \end{bmatrix} = B_0^{-1} \begin{bmatrix} \ddot{i}_d^* - \hat{\psi}_1(\cdot) - \varsigma_1\hat{S}_{FO1} - \phi_1 tanh(\hat{S}_{FO1}, \varepsilon_c) \\ \ddot{i}_q^* - \hat{\psi}_2(\cdot) - \varsigma_2\hat{S}_{FO2} - \phi_2 tanh(\hat{S}_{FO2}, \varepsilon_c) \end{bmatrix} \quad (43)$$

where ς_1, ς_2, ϕ_1, and ϕ_2 are positive control gains.

Remark 2. Modelling errors usually emerge from unknown SMES system parameters and unmodelled SMES dynamics, as well as external disturbances resulted from stochastic renewable energy penetration, which are all aggregated into perturbation and then estimated by SMSPO. The next step is to compensate the estimate online via AFOSMC, while the control structure of AFOSMC for PWM-CSC based SMES system is demonstrated in Fig. 5.

Remark 3. Note that perturbation observer (PO) based control design includes a large family of various control strategies that incorporated with PO. After the perturbation is estimated by PO, different controller can be employed to compensate the perturbation estimate. Thus far, authors have developed other controllers into this framework, e.g., perturbation observer based sliding-mode control (POSMC) for doubly-fed induction generator (DFIG) [26], perturbation estimation based robust state feedback control (PERSFC) for DFIG [27], as well as perturbation observer based fractional-order PID (PoFoPID) for photovoltaic inverters [36].

5. Case studies

Fig. 6 demonstrates the topology of a PWM-CSC based SMES system connected to a distribution network associated with renewable energy. Meanwhile, renewable energy is synthesized into distribution network at Bus 1. Moreover, Table 1 illustrates system parameters while Table 2 demonstrates the parameters of each controller, which structure is given in Appendix. Four case studies are implemented for the sake of verifying and comparing
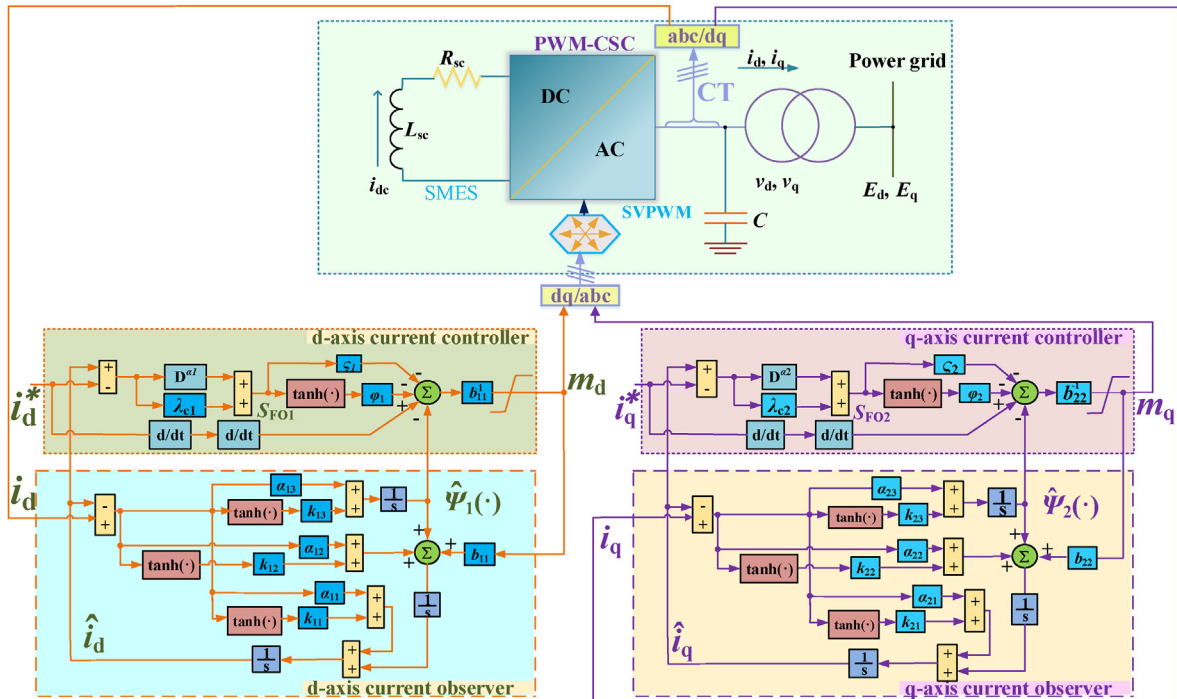

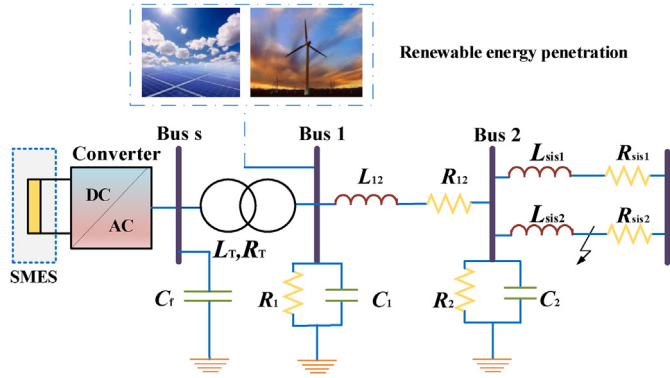**Fig. 5.** Overall AFOSMC control structure for PWM-CSC based SMES system.

Fig. 6. The topology of distribution network interconnected with PWM-CSC based SMES system and renewable energy.

Table 1
The parameters of SMES system and distribution network [20].

Parameter	Value	Unit	Parameter	Value	Unit	Parameter	Value	Unit
L_{sis1}, L_{sis2}	2.5	mH	R_{sis1}, R_{sis2}	5	mΩ	R_2	1	Ω
L_{12}	1.5	mH	R_{12}	10	mΩ	C	160	μF
L_T	2.5	mH	R_T	1.25	mΩ	C_2	0.1	μF
R_1	1	Ω	C_1	0.1	μF	v_{LL}^{rms}	440	V
C_2	0.1	μF	v_{LL}^{rms}	440	V	L_{SC}	7.5	H
R_{SC}	0.01	Ω	i_{dc}^{min}	20	A	i_{dc}^{max}	120	A
i_{dc}^{rated}	100	A	S_{SMES}^{rated}	37.5	kVA	Load	30	kW

the feasibility and merits of AFOSMC to that of traditional PID control [15], IDA-PBC [20], SMC [50], and FOSMC [37], respectively.

5.1. Active power and reactive power supply

This case aims to verify that SMES system is capable of supporting the active and reactive power when system operates under various circumstances. Here, power references keep changing and the major task is to accurately track them. Besides, the responses of system acquired via various controllers are demonstrated in Fig. 7. From which one can readily observe that AFOSMC can regulate both active and reactive power at the fastest rate without any overshoot.

5.2. System restoration capability under power grid fault

Faults occurred in power grid are very common that are usually result ed from extreme or severe weather, equipment defects, or improper management and maintenance, which may lead to an instantaneous power unbalance. Hence, control system requires to restore the perturbed system quickly and effectively [38,39]. Assume that between Bus 2 and infinite bus, a three-phase short-circuit fault happens on one transmission line at $t = 0.5$ s. Moreover, at $t = 0.6$ s, the faulty line is disconnected, and switched on and

restore normal power supply when the automatic reclosing devices clear the fault [40].

Fig. 8 demonstrates restoration performance acquired by different controllers when fault occurs. One can easily find that AFOSMC is capable of efficiently and significantly alleviating power oscillations resulted from the fault and ensuring the unstable system to be restored to normal operation condition at the highest rate. Besides, the perturbation estimation performance of SMSPO during the power grid fault period is also monitored. One can observe that perturbations can be efficiently estimated in roughly 250 ms.

5.3. Power support under random renewable energy penetration

This scenario investigates the power support performance under random renewable energy penetration [41,42]. A total capacity of 3 kW renewable energy (a mixed 1.5 kW wind energy and 1.5 kW solar energy) is applied. Note that active power production is actually time-varying due to inherent randomness of renewable energy resources [43]. Hence, it requires SMES system to rapidly compensate the malignant oscillations of active power resulted from the change of wind speed and solar irradiation variations, and to offer reactive power required by induction machines [44] to guarantee the power factor of Bus 1. Fig. 9 shows that undesirable active/reactive power oscillations could be significantly reduced by AFOSMC, hence the system stability can be considerably enhanced.

5.4. Robustness with system parameter uncertainties

A range of plant-model mismatches of the equivalent resistance R_{eq} and inductance L_{eq} with ±10% difference compared with their normal value have been undertaken. Particularly, it is noteworthy that such parameter uncertainties could be resulted from aging, overheating, as well as inaccurate measurement. Then, at infinite bus, a 30% voltage drop caused by power grid faults is simulated lasting round 100 ms, while peak value of active power $|P_{ac}|$ is recorded. Fig. 10 shows the change of $|P_{ac}|$ by PID control, IDA-PBC, SMC, FOSMC, and AFOSMC is 40.3%, 79.7%, 27.6%, 25.4%, and 15.6%, respectively. Consequently, AFOSMC possesses the greatest robustness among all controllers under system parameter uncertainties.

5.5. Comparative studies

For the purpose of quantitatively evaluating the control performance, integral of absolute error (IAE) [45–48] obtained under three cases are given in Table 3. One can find that IAE indices of AFOSMC are always the lowest under all circumstances, which demonstrates that its control performance is the best. Particularly, its IAE_{Pac} is only 63.55%, 83.44%, 69.60%, and 76.67% to that of PID control, IDA-PBC, SMC, and FOSMC in terms of power supply, respectively. Meanwhile, its IAE_{Qac} is just 55.29%, 73.90%, 58.78%, and 66.01% to that of PID control, IDA-PBC, SMC, and FOSMC in

Table 2
The parameters of each controller.

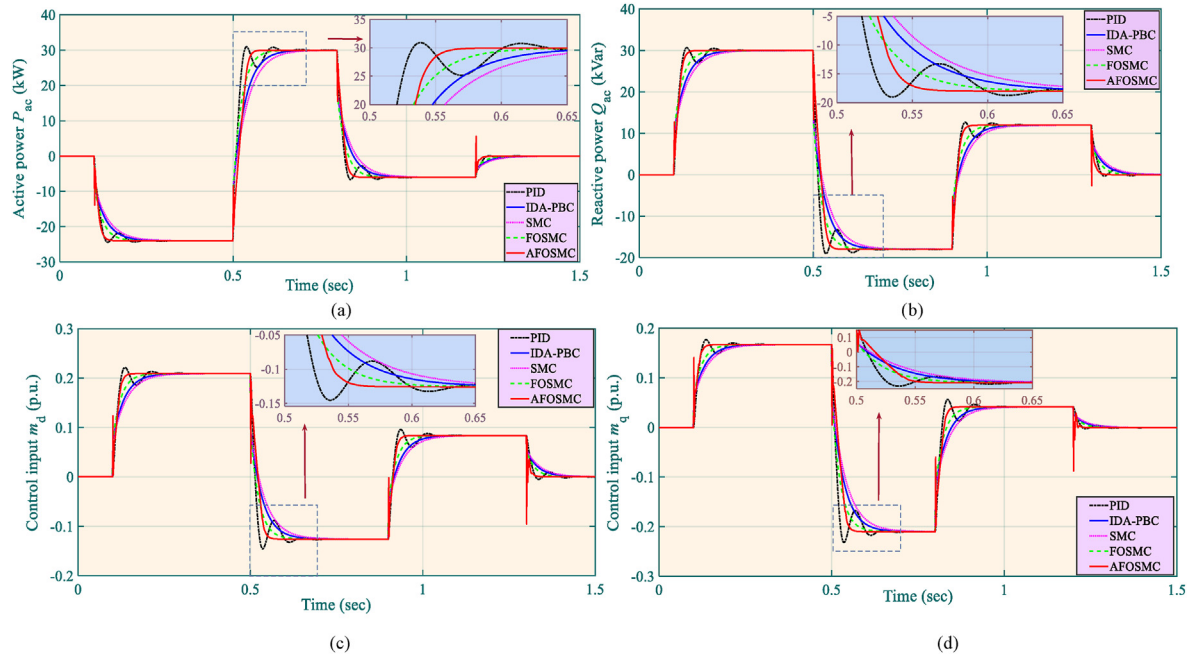| controllers	parameters								
PID	$K_{P1} = 100$	$K_{I1} = 250$	$K_{D1} = 15$	$K_{P2} = 75$	$K_{I2} = 200$	$K_{D2} = 10$			
IDA-PBC	$R_1 = 45$	$R_2 = 45$	$R_3 = 35$	$k_1 = 4$	$k_2 = 3$	$k_3 = 2$	$k_4 = 2$		
SMC	$\varsigma_1 = 25$	$\phi_1 = 21$	$\varepsilon_o = 0.2$	$\phi_2 = 20$	$\lambda_{c1} = 25$	$\lambda_{c2} = 20$	$\varepsilon_c = 0.2$		
FOSMC	$\varsigma_1 = 20$	$\varsigma_2 = 15$	$\phi_1 = 25$	$\phi_2 = 20$	$\lambda_{c1} = 25$	$\lambda_{c2} = 20$	$\alpha1 = 0.8$	$\alpha2 = 0.5$	$\varepsilon_c = 0.2$
AFOSMC	$\alpha_{11} = 30$	$\alpha_{12} = 300$	$\alpha_{13} = 1000$	$\alpha_{21} = 30$	$\alpha_{22} = 300$	$\alpha_{23} = 100$	$b_{11} = 500$	$b_{22} = 600$	$\varepsilon_c = 0.2$
	$\varsigma_1 = 15$	$\varsigma_2 = 10$	$\phi_1 = 20$	$\phi_2 = 15$	$\lambda_{c1} = 20$	$\lambda_{c2} = 15$	$\alpha1 = 0.8$	$\alpha2 = 0.5$	$\varepsilon_o = 0.2$
	$k_{11} = 20$	$k_{12} = 600$	$k_{13} = 6000$	$k_{21} = 20$	$k_{22} = 600$	$k_{23} = 6000$			

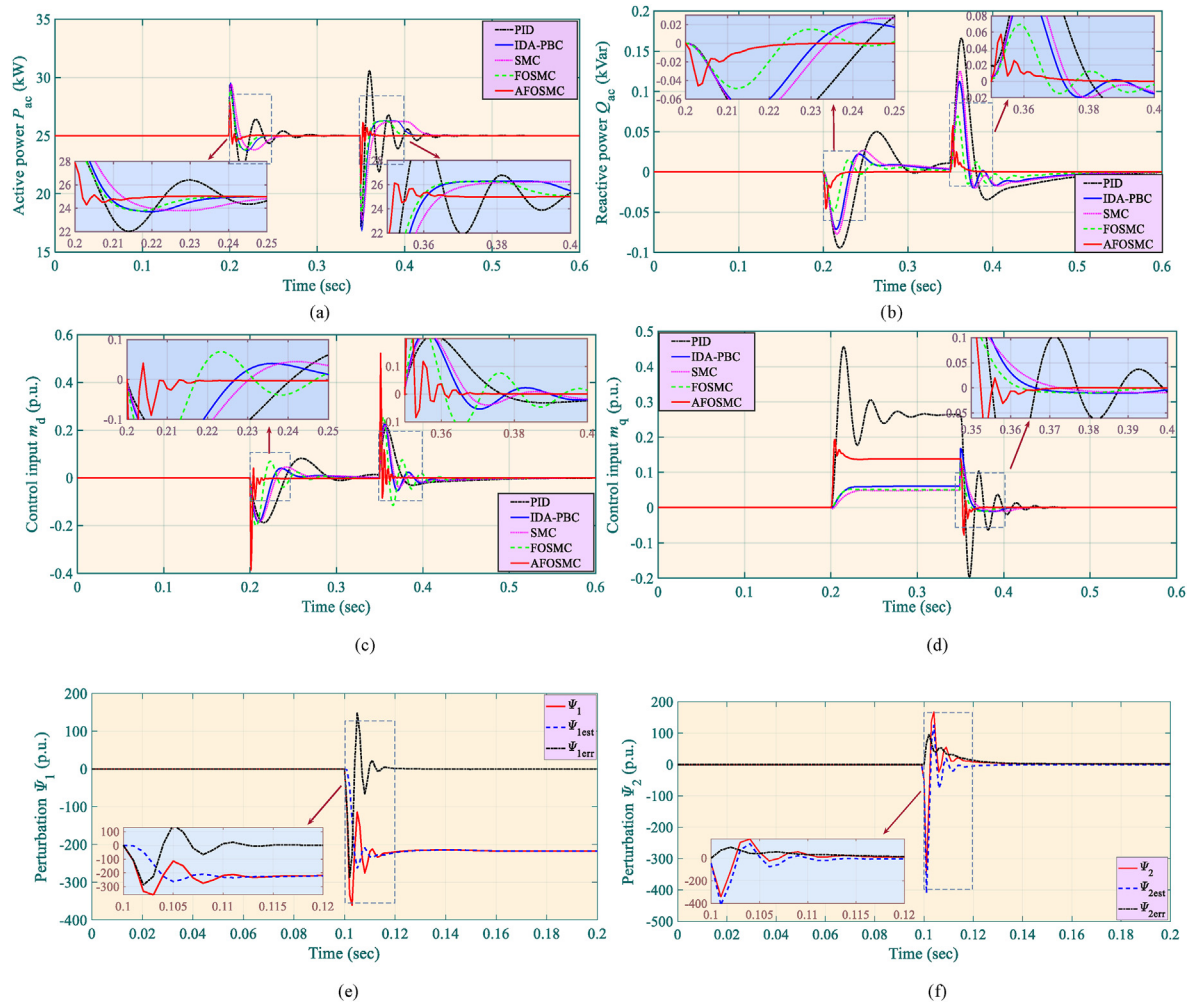**Fig. 7.** Simulation results acquired under active power and reactive power support.

Fig. 8. System restoration performance acquired under power system fault.
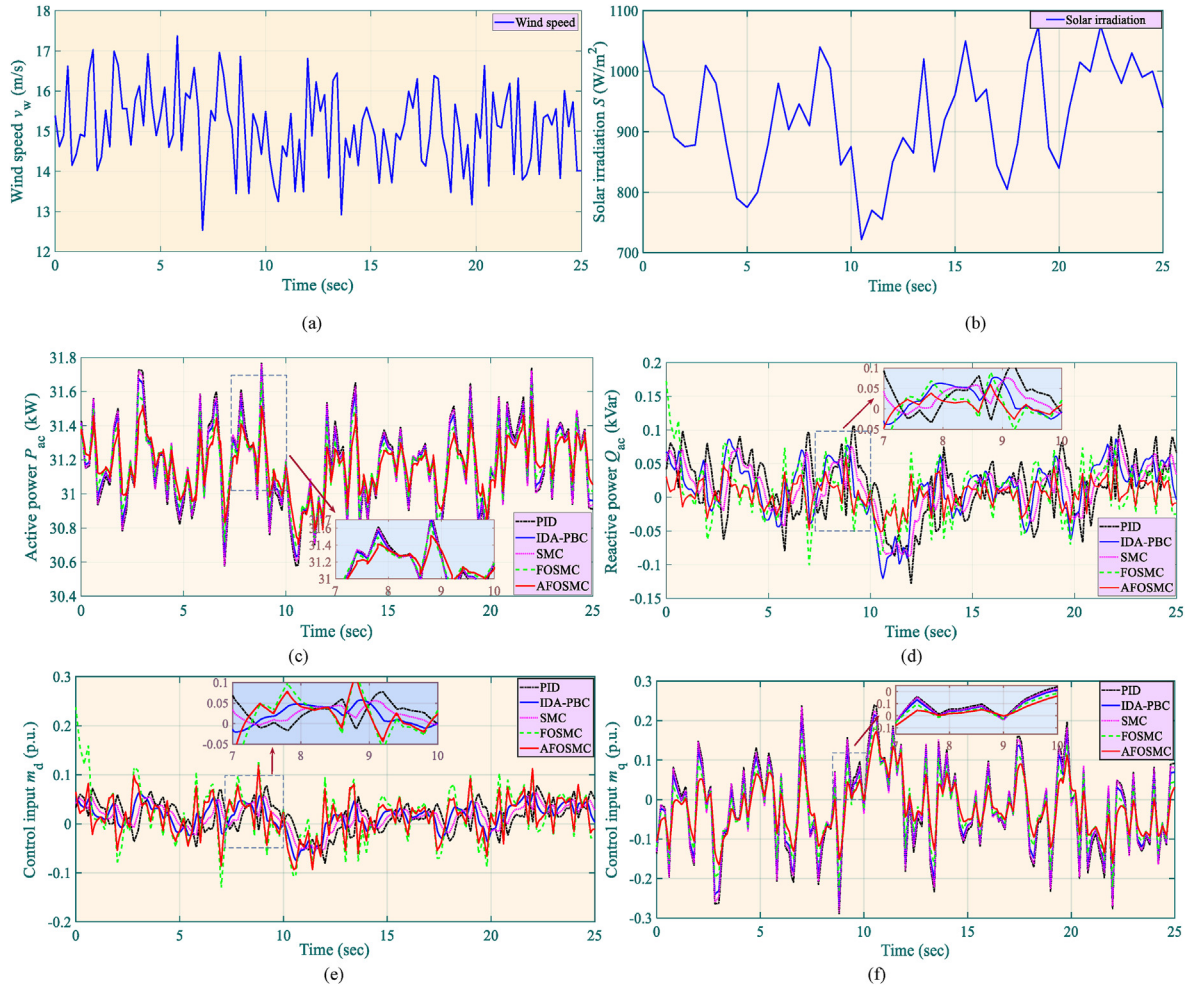
Fig. 9. Results acquired under random renewable energy penetration.

terms of system restoration, respectively.

Lastly, Table 4 compares the overall control costs [49–52] of each controller. It is obvious that the required costs of AFOSMC is the lowest under all circumstances. Besides, its control costs under power support uwith random renewable energy penetration are only 87.49%, 96.08%, 93.16%, and 94.37% to that of PID control, IDA-PBC, SMC, and FOSMC, respectively. Lastly, simulation results show that AFOSMC can greatly outperform other approaches in both tracking speed and overall costs, e.g., its active power error is only 63.55%, 83.44%, 69.60%, and 76.67% of that of PID control, IDA-PBC, SMC, and FOSMC under reactive and active power supply, while the required control costs is only 76.69%, 91.28%, 83.50, and 86.76% to the above three controllers.

Remark 4. Note that the control performance evaluation criteria include four aspects: (a) tracking error, (b) control costs, (c) robustness and (d) structure complexity, e.g., numbers of states/parameters that need to be measured. One can see from Table 3 (tracking error), Table 4 (control costs), Fig. 10 (robustness), Eqs. (40)-(43) and Appendix (structure complexity) that AFOSMC owns the best control performance among all controllers.

Remark 5. Other state-of-the-art PID control, called optimal passive fractional-order PID (OPFoPID) control [53], has also been compared to further evaluate the control performance of AFOSMC. It has been found that AFOSMC outperforms OPFoPID control in all the three cases, e.g., its IAE_{Pac} and IAE_{Qac} obtained under active power and reactive power supply are just 92.64% and 97.27% to that of OPFoPID control. More importantly, AFOSMC only requires the measurement of dq-axis currents while OPFoPID control requires many SMES system states/parameters to be measured. Besides, AFOSMC owns much higher robustness and less control costs than that of OPFoPID control. As a result, AFOSMC shows superior control performance in all evaluation criteria described in Remark 4 in comparison to that of OPFoPID control.

6. HIL test

This section aims to further investigate the implementation feasibility of AFOSMC. An HIL experiment based on dSpace platform is implemented while its configuration and platform are depicted in Fig. 11 and Fig. 12, respectively. Besides, SMES system (1)−(7) has been embedded on DS1006 platform while the sampling frequency is f_s = 100 kHz. Furthermore, AFOSMC (40)−(43) has been
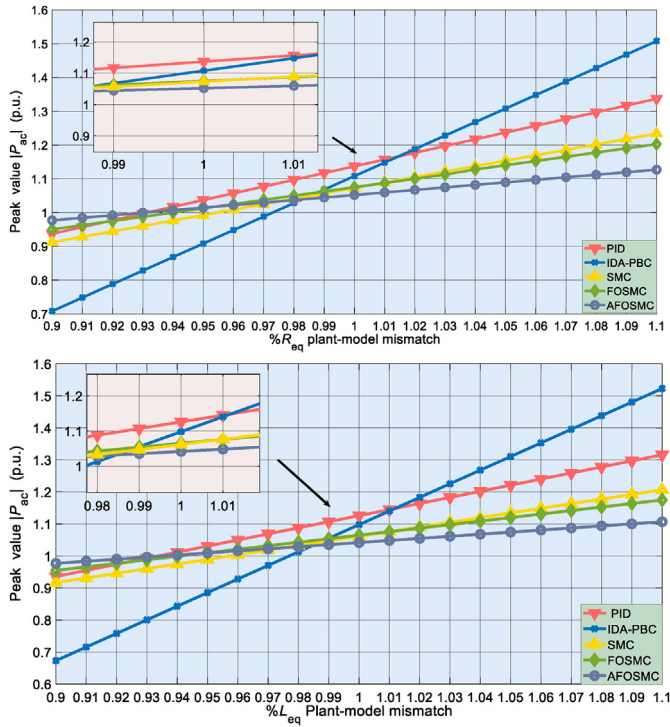
Fig. 10. Robustness results obtained under a 30% voltage drop.

Fig. 11. The configuration of HIL test.

implemented on DS1104 platform whose sampling frequency is $f_c = 5$ kHz.

Fig. 13 depicts the results of simulation and HIL under reactive and active power supply. It can be easily found that their results are quite similar. Note that there exist some consistent power oscillations with a magnitude of 3.5 kW in active power and 2.5 kVar in reactive power in HIL experiment.

Then, simulation and HIL results acquired by system restoration is illustrated in Fig. 14. Clearly, their responses are quite close. It can
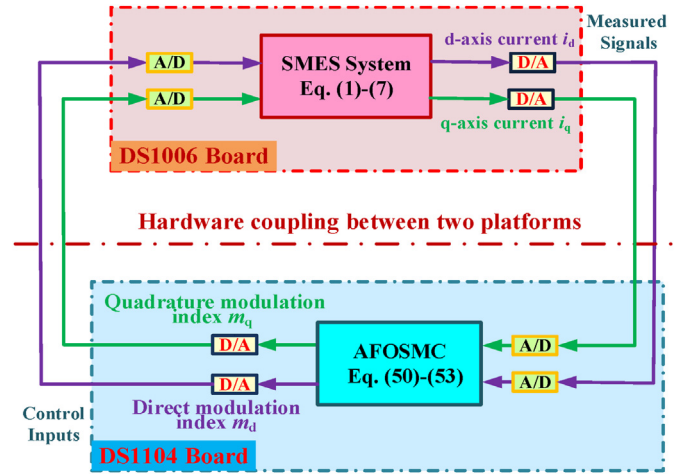
be seen that some insignificant power oscillations appear in HIL experiment, with a magnitude of 0.023 kW in active power and 0.014 kVar in reactive power at their steady state.

In Fig. 15, power support under random renewable energy penetration of simulation and HIL test is compared, which have very similar curves. One can observe that a 0.35 kW active power oscillation and 0.04 kVar reactive power oscillation emerge in HIL test.

Note that the difference between simulation and HIL is mainly caused by the followings:

- *Time delay*: It often leads to a degradation of the desired control performance, e.g., simulation response is faster than that of HIL by around 0.02 s in Fig. 13;

Table 3
IAE indices (in p.u.) of each controller acquired under five conditions.

Conditions	IAE Indices	PID	IDA-PBC	SMC	FOSMC	AFOSMC
Active power and reactive power supply	IAE_{Pac}	0.2735	0.2083	0.2497	0.2267	**0.1738**
	IAE_{Qac}	0.2941	0.2114	0.2638	0.2346	**0.1851**
System restoration capability under power grid fault	IAE_{Pac}	0.1758	0.1303	0.1609	0.1485	**0.1069**
	IAE_{Qac}	0.1823	0.1364	0.1715	0.1527	**0.1008**
Power support under wind energy penetration	IAE_{Pac}	0.3764	0.3196	0.3518	0.3342	**0.2645**
	IAE_{Qac}	0.3925	0.3328	0.3706	0.3529	**0.2819**
Power support under solar energy penetration	IAE_{Pac}	0.3057	0.2409	0.2736	0.2497	**0.1986**
	IAE_{Qac}	0.3211	0.2628	0.2923	0.2708	**0.2118**
Power support under mixed wind/solar energy penetration	IAE_{Pac}	0.4579	0.3536	0.3918	0.3729	**0.3122**
	IAE_{Qac}	0.4728	0.3657	0.4022	0.3833	**0.3246**

Table 4
Overall control costs (in p.u.) of each controller acquired under five conditions.

| Conditions	PID	IDA-PBC	SMC	FOSMC	AFOSMC
Active power and reactive power supply	0.3947	0.3316	0.3625	0.3489	**0.3027**
System restoration under power grid fault	0.2628	0.2275	0.2507	0.2356	**0.1964**
Power support under wind energy penetration	0.7653	0.7198	0.7524	0.7348	**0.6861**
Power support under solar energy penetration	0.6278	0.5719	0.6093	0.5877	**0.5388**
Power support under mixed wind/solar energy penetration	0.8579	0.7812	0.8057	0.7954	**0.7506**
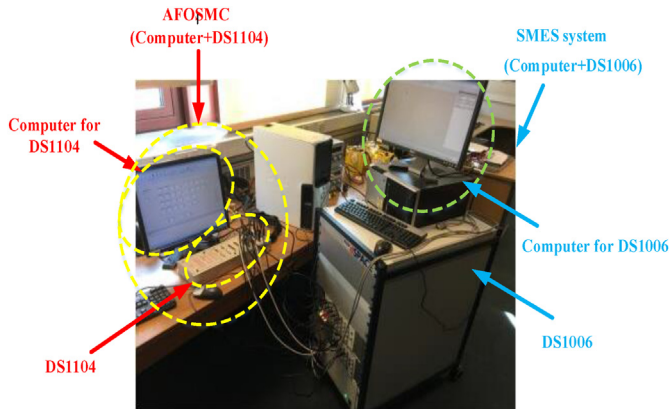
Fig. 12. The hardware schematic of HIL experiment.

- *Measurement disturbance*: It usually results in consistent oscillations in HIL test, as discussed above;
- *Discretization of HIL test and sampling holding*: It generally brings in an additional amount of errors against that of continuous control used in simulation.

Lastly, it is worth noting that the application of SMES technology is still quite expensive at the moment, particularly at the real power grid level investigated in this study. As a result, this work can only validate the control performance of AFOSMC by HIL test due to limited resources. In fact, HIL test is a common and highly acceptable tool to test new controller design in power system industries before it can be finally implemented in industrial applications.

7. Conclusions

This paper firstly estimates the combined effect of modelling uncertainties, unknown parameters, and external disturbances of SMES system via an SMSPO, which is then fully compensated by FOSMC. Hence, considerable robustness can be realized. Besides, more reasonable control efforts are resulted in because of the utilization of real-time estimate of perturbation instead of its upper bound adopted by SMC. Under the proposed control framework, only dq-axis currents need to be measured thus the overall computation/measurement costs of AFOSMC is relatively low. Meanwhile, the utilization of fractional-order sliding surface can considerably improve the dynamic responses. In addition, continuous function tanh(.) replaces discontinuous function sgn(.), thus the chattering effect can be largely suppressed. Three scenarios are studied to verify and compare the feasibility and merits of AFOSMC to that of four controllers. Furthermore, a dSpace based HIL test is implemented to verify its feasibility under practical scenarios.

Future studies will be focused on the application of AFOSMC on real SMES systems used in power systems to further test its effectiveness in industrial experiment and including the electric vehicle into the studied system.

Declaration of competing interest

I can hereby confirm there is no interests conflict of the work to anyone.

CRediT authorship contribution statement

Bo Yang: Conceptualization, Writing - original draft. **Junting Wang:** Investigation. **Xiaoshun Zhang:** Methodology. **Lei Yu:** Data curation. **Hongchun Shu:** Supervision. **Tao Yu:** Resources. **Liming**
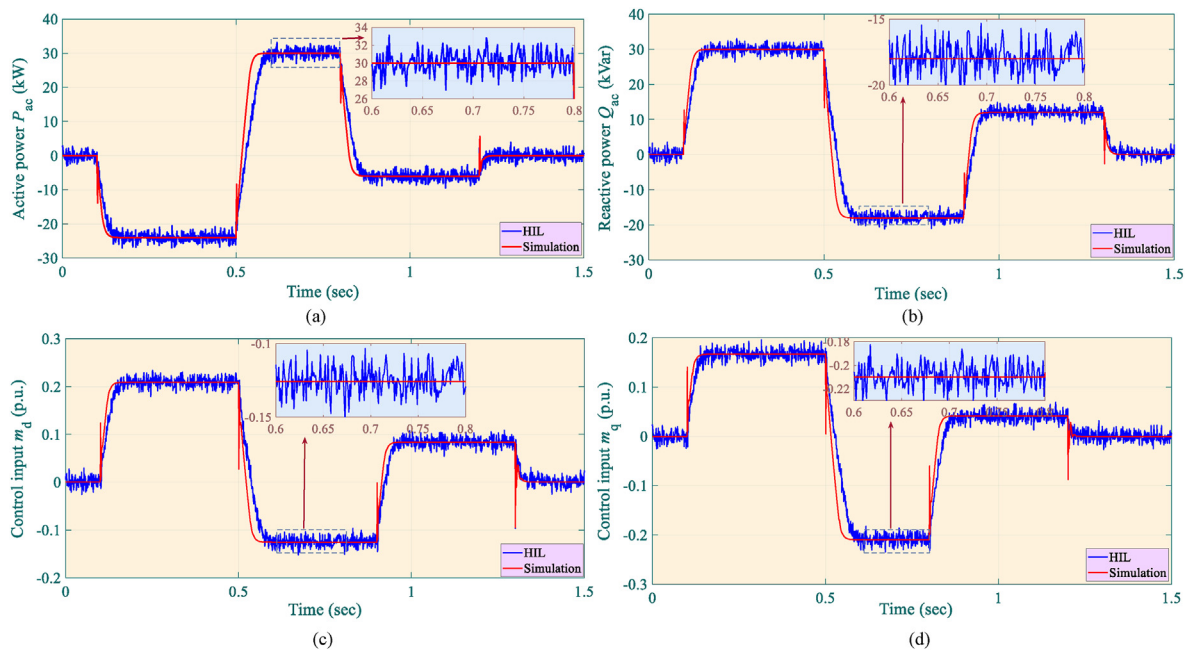

Fig. 13. Results of simulation and HIL experiment obtained under active power and reactive power supply.
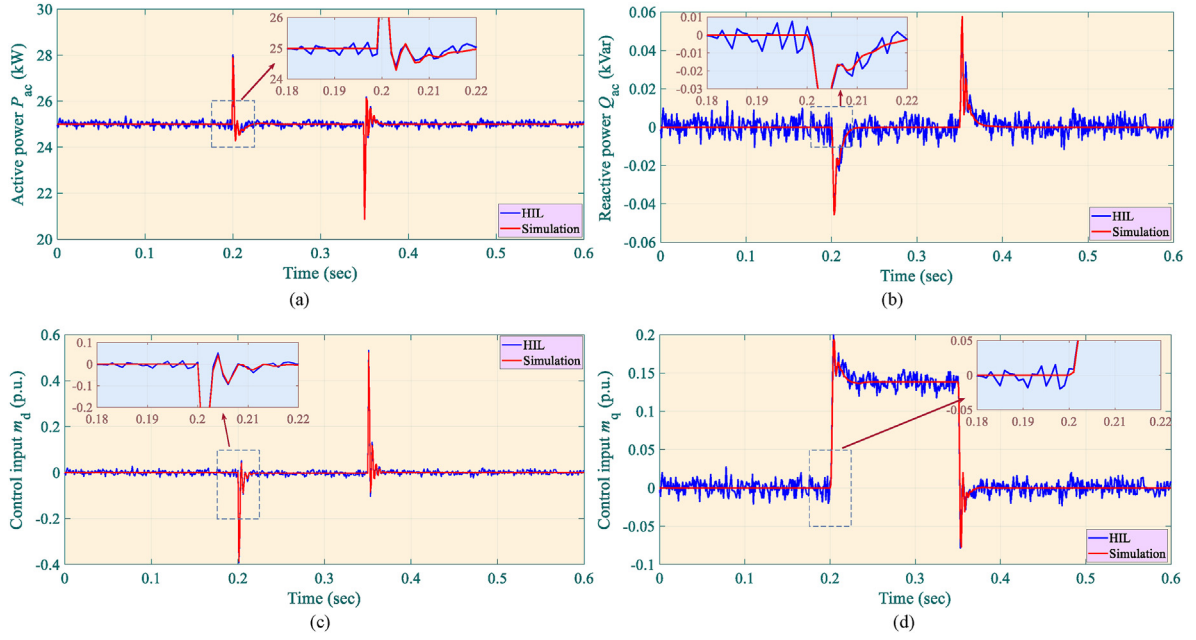
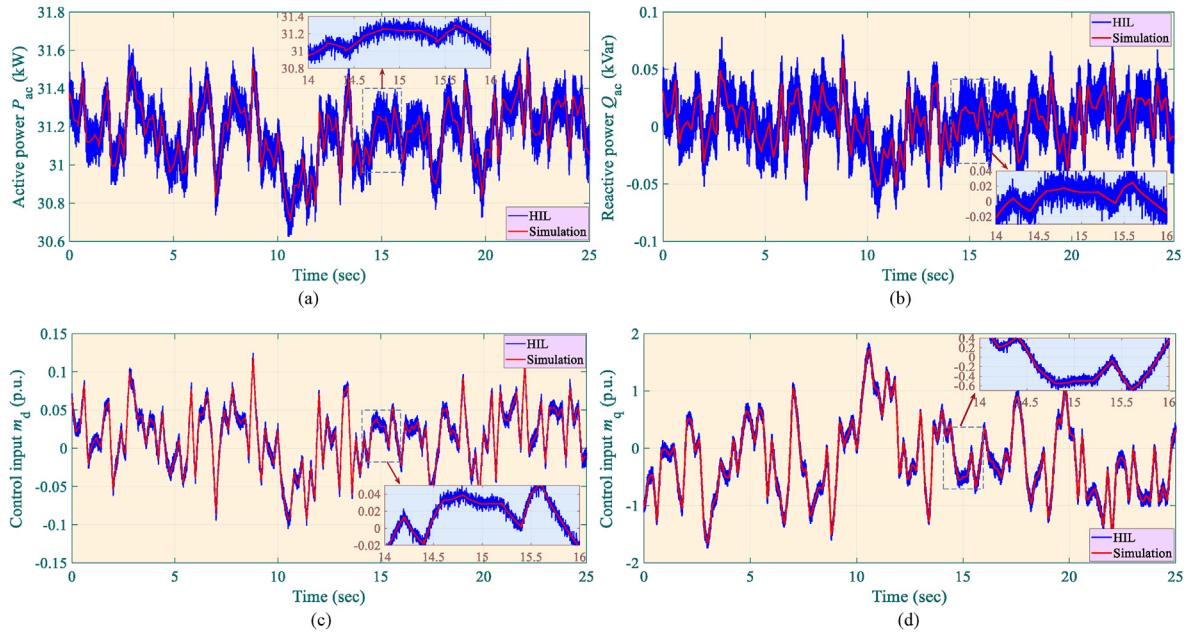**Fig. 14.** Results of simulation and HIL experiment obtained under power grid fault.

Fig. 15. Results of simulation and HIL experiment obtained under power support with random renewable energy penetration.

Sun: Writing - review & editing.

Appendix A. Structure of comparative controllers

Note that d-axis current reference i_d^* and q-axis current reference i_q^* are given from Eq. (26) and Eq. (27). The detailed structure of other four controllers (AFOSMC has been given in Eqs. (40)-(43))

are given as follows:

(a) PID control [15]:

$$\begin{cases} m_d = K_{P1}\left(i_d - i_d^*\right) + K_{I1}\int\left(i_d - i_d^*\right)\mathrm{d}t + K_{D1}\dfrac{\mathrm{d}}{\mathrm{d}t}\left(i_d - i_d^*\right) \\ m_q = K_{P2}\left(i_q - i_q^*\right) + K_{I2}\int\left(i_q - i_q^*\right)\mathrm{d}t + K_{D2}\dfrac{\mathrm{d}}{\mathrm{d}t}\left(i_q - i_q^*\right) \end{cases} \quad (A1)$$

(b) IDA-PBC [20]:

$$
\begin{cases}
m_d = \dfrac{1}{i_{dc}}\left[wCv_q^* + \dfrac{E_d P_{ac}^* \beta + E_q Q_{ac}^*}{E_d^2 + E_q^2} + wC1 - k_4\left(v_q - v_q^*\right) - R_3\left(v_d - v_d^*\right) \right. \\
\qquad\qquad \left. -(k_3 - 1)\left(i_d - \dfrac{E_d P_{ac}^* \beta + E_q Q_{ac}^*}{E_d^2 + E_q^2}\right)\right] \\[2em]
m_q = -\dfrac{1}{i_{dc}}\left[wCv_d^* - \dfrac{E_d P_{ac}^* \beta - E_q Q_{ac}^*}{E_d^2 + E_q^2} + wC1 - k_4\left(v_d - v_d^*\right) + R_4\left(v_q - v_q^*\right) \right. \\
\qquad\qquad \left. +(k_2 - 1)\left(i_q - \dfrac{E_d P_{ac}^* \beta - E_q Q_{ac}^*}{E_d^2 + E_q^2}\right)\right]
\end{cases}
$$

(A2)

with

$$
\begin{cases}
v_d^* = \dfrac{1}{k_3}\left[E_d + \dfrac{wL_T(E_d P_{ac}^* \beta - E_q Q_{ac}^*) + R_T(E_d P_{ac}^* \beta + E_q Q_{ac}^*)}{E_d^2 + E_q^2} - R_1\left(i_d - \dfrac{E_d P_{ac}^* \beta + E_q Q_{ac}^*}{E_d^2 + E_q^2}\right) \right. \\
\qquad\qquad \left. + wL_T 1 - k_1\left(i_q - \dfrac{E_d P_{ac}^* \beta - E_q Q_{ac}^*}{E_d^2 + E_q^2}\right) + v_d(k_3 - 1)\right] \\[2em]
v_q^* = \dfrac{1}{k_4}\left[E_q - \dfrac{wL_T(E_d P_{ac}^* \beta - E_q Q_{ac}^*) + R_T(E_d P_{ac}^* \beta + E_q Q_{ac}^*)}{E_d^2 + E_q^2} - R_2\left(i_q - \dfrac{E_d P_{ac}^* \beta - E_q Q_{ac}^*}{E_d^2 + E_q^2}\right) \right. \\
\qquad\qquad \left. - wL_T 1 - k_1\left(i_d - \dfrac{E_d P_{ac}^* \beta + E_q Q_{ac}^*}{E_d^2 + E_q^2}\right) + v_q(k_2 - 1)\right]
\end{cases}
$$

(A3)

(c) SMC [50]:

$$
\begin{cases}
m_d = \dfrac{CL_T}{i_{dc}}\left[\ddot{i}_d^* + \left(\dfrac{1}{CL_T} - \dfrac{R_T^2}{L_T^2} + \omega^2\right)i_d - \dfrac{2\omega R_T}{L_T}i_q - \dfrac{R_T}{L_T^2}(E_d - v_d) - \dfrac{w}{L_T}E_q + \dfrac{2w}{L_T}v_q + \dfrac{1}{L_T}\dot{E}_d - \varsigma_1 S_1 - \phi_1 \tanh(S_1, \varepsilon_c) \right] \\[1em]
m_q = \dfrac{CL_T}{i_{dc}}\left[\ddot{i}_q^* + \left(\dfrac{1}{CL_T} - \dfrac{R_T^2}{L_T^2} + \omega^2\right)i_q + \dfrac{2\omega R_T}{L_T}i_q - \dfrac{R_T}{L_T^2}(E_q - v_q) + \dfrac{w}{L_T}E_d - \dfrac{2w}{L_T}v_d + \dfrac{1}{L_T}\dot{E}_q - \varsigma_2 S_2 - \phi_2 \tanh(S_2, \varepsilon_c) \right]
\end{cases}
$$

(A4)

with

$$
\begin{bmatrix} S_1 \\ S_2 \end{bmatrix} = \begin{bmatrix} \dfrac{d}{dt}(i_d - i_d^*) + \lambda_{c1}(i_d - i_d^*) \\[1em] \dfrac{d}{dt}(i_q - i_q^*) + \lambda_{c2}(i_q - i_q^*) \end{bmatrix}
$$

(A5)

(d) FOSMC [37]:

$$
\begin{cases}
m_d = \dfrac{CL_T}{i_{dc}}\left[\ddot{i}_d^* + \left(\dfrac{1}{CL_T} - \dfrac{R_T^2}{L_T^2} + \omega^2\right)i_d - \dfrac{2\omega R_T}{L_T}i_q - \dfrac{R_T}{L_T^2}(E_d - v_d) - \dfrac{w}{L_T}E_q + \dfrac{2w}{L_T}v_q + \dfrac{1}{L_T}\dot{E}_d - \varsigma_1 S_{FO1} - \phi_1 \tanh(S_1, \varepsilon_c) \right] \\[1em]
m_q = \dfrac{CL_T}{i_{dc}}\left[\ddot{i}_q^* + \left(\dfrac{1}{CL_T} - \dfrac{R_T^2}{L_T^2} + \omega^2\right)i_q + \dfrac{2\omega R_T}{L_T}i_q - \dfrac{R_T}{L_T^2}(E_q - v_q) + \dfrac{w}{L_T}E_d - \dfrac{2w}{L_T}v_d + \dfrac{1}{L_T}\dot{E}_q - \varsigma_2 S_{FO2} - \phi_2 \tanh(S_2, \varepsilon_c) \right]
\end{cases}
$$

(A6)

with

$$
\begin{bmatrix} S_{FO1} \\ S_{FO2} \end{bmatrix} = \begin{bmatrix} D^{\alpha 1}\left(\widehat{\dot{i}}_d - \dot{i}_d^*\right) + \lambda_{c1}\left(\widehat{i}_d - \dot{i}_d^*\right) \\[1em] D^{\alpha 2}\left(\dot{i}_q - \dot{i}_q^*\right) + \lambda_{c2}\left(\dot{i}_q - \dot{i}_q^*\right) \end{bmatrix}
$$

(A7)

References

[1] Olabi AG. Renewable energy and energy storage systems. Energy 2017;136: 1–6.

[2] Hua HC, Qin YC, Hao CT, Cao JW. Optimal energy management strategies for energy Internet via deep reinforcement learning approach. Appl Energy 2019;239:598–609.

[3] Yang B, Zhang XS, Yu T, Shu HC, Fang ZH. Grouped grey wolf optimizer for maximum power point tracking of doubly-fed induction generator based wind turbine. Energy Convers Manag 2017;133:427–43.

[4] Yang B, Wang JB, Zhang XS, Yu T, Yao W, Shu HC, Zeng F, Sun LM. Comprehensive overview of meta-heuristic algorithm applications on PV cell parameter identification. Energy Convers Manag 2020;208:112595.

[5] Yang B, Yu T, Shu HC, Zhang YM, Chen J, Sang YY, Jiang L. Passivity-based sliding-mode control design for optimal power extraction of a PMSG based variable speed wind turbine. Renew Energy 2018;119:577–89.

[6] McPherson M, Tahseen S. Deploying storage assets to facilitate variable renewable energy integration: the impacts of grid flexibility, renewable penetration, and market structure. Energy 2018;145:856–70.

[7] Antonio CS, Enrique-Luis MI, Enrique RA. Africa Lopez-Rey. technical approach for the inclusion of superconducting magnetic energy storage in a smart city. Energy 2018;158:1080–91.

[8] Obara S, Sato K, Utsugi Y. Study on the operation optimization of an isolated island microgrid with renewable energy layout planning. Energy 2018;161: 1211–25.

[9] Ruan J, Song Q, Yang WW. The application of hybrid energy storage system with electrified continuously variable transmission in battery electric vehicle. Energy 2019;183:315–30.

[10] Shi J, Xu Y, Liao M, Guo SQ, Li YY, Ren L, Su RY, Li SJ, Zhou X, Tang YJ. Integrated design method for superconducting magnetic energy storage considering the high frequency pulse width modulation pulse voltage on magnet. Appl Energy 2019;248:1–17.

[11] Daniel Á, Rafael A, José AA. Sizing and operation of hybrid energy storage systems to perform ramp-rate control in PV power plants. Electrical Power and Energy Systems 2019;107:589–96.

[12] Vulusala GVS, Madichetty S. Application of superconducting magnetic energy storage in electrical power and energy systems: a review. Int J Energy Res 2018;42:358–68.

[13] Colmenar-Santos A, Luis-Molina E, Rosales-Asensio E, Lopez-Rey Á. Technical approach for the inclusion of superconducting magnetic energy storage in a smart city. Energy 2018;158:1080–91.

[14] Ali MH, Wu B, Dougal RA. An overview of SMES applications in power and energy systems. IEEE Transactions on Sustainable Energy 2010;1(1):38–47.

[15] Ortega A, Milano F. Generalized model of VSC-based energy storage systems for transient stability analysis. IEEE Trans Power Syst 2016;31(5):3369–80.

[16] Lin XD, Lei Y, Zhu YW. A novel superconducting magnetic energy storage system design based on a three-level T-type converter and its energy-shaping control strategy. Elec Power Syst Res 2018;162:64–73.

[17] Wang S, Jin J. Design and analysis of a fuzzy logic controlled SMES system. IEEE Trans Appl Supercond 2014;24(5):1–5.

[18] Trilochan P, Anup KP, Sunil KS. Implementing dynamic evolution control approach for DC-link voltage regulation of superconducting magnetic energy storage system. Electrical Power and Energy Systems 2018;95:275–86.

[19] Shi J, Tang Y, Ren L, Li J, Cheng S. Discretization-based decoupled state-feedback control for current source power conditioning system of SMES. IEEE Trans Power Deliv 2008;23(4):2097–104.

[20] Montoya OD, Alejandro G, Gerardo EP. A generalized passivity-based control approach for power compensation in distribution systems using electrical energy storage systems. Journal of Energy Storage 2018;16:259–68.

[21] Wan Y, Zhao J. Extended backstepping method for single-machine infinite-bus power systems with SMES. IEEE Trans Contr Syst Technol 2013;21(3):915–23.

[22] Elsisi M, Soliman M, Aboelela M, Mansour W. Optimal design of model predictive control with superconducting magnetic energy storage for load frequency control of nonlinear hydrothermal power system using bat inspired algorithm. Journal of Energy Storage 2017;12:311–8.

[23] Shtessel Y, Baev S, Biglari H. Unity power factor control in three-phase AC/DC boost converter using sliding modes. IEEE Trans Ind Electron 2008;55(11): 3874–82.

[24] Yang B, Yu T, Shu HC, Zhu DN, An N, Sang YY, Jiang L. Perturbation observer based fractional-order sliding-mode controller for MPPT of grid-connected PV inverters: design and real-time implementation. Contr Eng Pract 2018;79: 105–25.

[25] Yang B, Zhu TJ, Zhang XS, Wang JB, Shu HC, Li SN, He TY, Yang L, Yu T. Design and implementation of battery/SMES hybrid energy storage systems used in electric vehicles: a nonlinear robust fractional-order control approach. Energy 2020;191:116510.

[26] Yang B, Yu T, Shu HC, Dong J, Jiang L. Robust sliding-mode control of wind energy conversion systems for optimal power extraction via nonlinear perturbation observers. Appl Energy 2018;210:711–23.

[27] Yang B, Hu YL, Huang HY, Shu HC, Yu T, Jiang L. Perturbation estimation based robust state feedback control for grid connected DFIG wind energy conversion system. Int J Hydrogen Energy 2017;42(33):20994–1005.

[28] Jiang L, Wu QH, Wen JY. Nonlinear adaptive control via sliding-mode state and perturbation observer. IEE Proc Contr Theor Appl 2002;149:269–77.

[29] Morandi A. Design and comparison of a 1-MW/5-s HTS SMES with toroidal and solenoidal geometry. IEEE Trans Appl Supercond 2016;26(4):1–6.

[30] Vnlusala GVS, Madichetty S. Application of superconducting magnetic energy storage in electrical power and energy systems: a review. Int J Energy Res 2018;42:358–68.

[31] Giraldo E, Garces A. An adaptive control strategy for a wind energy conversion system based on PWM-CSC and PMSG. IEEE Trans Power Syst 2014;29(3): 1446–53.

[32] Espinoza JR, Joos G. State variable decoupling and power flow control in PWM current-source rectifiers. IEEE Trans Ind Electron 1998;45(1):78–87.

[33] Elwakil SA, El-Labany SK, Zahran MA, Sabry R. Modified extended tanh-function method and its applications to nonlinear equations. Appl Math Comput 2005;161(2):403–12.

[34] Podlubny I. Fractional differential equations. New York: Academic Press; 1999.

[35] Matignon D. Stability properties for generalized fractional differential systems. ESAIM Proc 1998;5(5):145–58.

[36] Yang B, Yu T, Shu HC, Zhu DN, Zeng F, Sang YY, Jiang L. Perturbation observer based fractional-order PID control of photovoltaics inverters for solar energy harvesting via Yin-Yang-Pair optimization. Energy Convers Manag 2018;171: 170–87.

[37] Calderón AJ, Vinagre BM, Feliu V. Fractional order control strategies for power electronic buck converters. Signal Process 2006;86(10):2803–19.

[38] Shen Y, Yao W, Wen JY, He HB, Jiang L. Resilient wide-area damping control using GrHDP to tolerate communication failures. IEEE Transactions on Smart Grid 2019;10(3):2547–57.

[39] Chen J, Yao W, Zhang CK, Ren Y, Jiang L. Design of robust MPPT controller for grid-connected PMSG-Based wind turbine via perturbation observation based nonlinear adaptive control. Renew Energy 2019;134:478–95.

[40] Liu J, Yao W, Wen JY, Fang JK, Jiang L, He HB, Cheng SJ. Impact of power grid strength and PLL parameters on stability of grid-connected DFIG wind farm. IEEE Transactions on Sustainable Energy 2020;11(1):545–57.

[41] Yang B, Jiang L, Wang L, Yao W, Wu QH. Nonlinear maximum power point tracking control and modal analysis of DFIG based wind turbine. Int J Electr Power Energy Syst 2016;74:429–36.

[42] Yang B, Zhong LE, Yu T, Li HF, Zhang XS, Shu HC, Sang YY, Jiang L. Novel bio-inspired memetic salp swarm algorithm and application to MPPT for PV systems considering partial shading condition. J Clean Prod 2019;215: 1203–22.

[43] Liao SW, Yao W, Han XN, Wen JY, Cheng SJ. Chronological operation simulation framework for regional power system under high penetration of renewable energy using meteorological data. Appl Energy 2017;203:816–28.

[44] Liu J, Wen JY, Yao W, Long Y. Solution to short-term frequency response of wind farms by using energy storage systems. IET Renew Power Gener 2016;10(5):669–78.

[45] Fang JK, Yao W, Chen Z, Wen JY, Su C, Cheng SJ. Improvement of wide-area damping controller subject to actuator saturations: a dynamic anti-windup approach. IET Gener, Transm Distrib 2018;12(9):2115–23.

[46] Injeti SK, Thunuguntla VK. Optimal integration of DGs into radial distribution network in the presence of plug-in electric vehicles to minimize daily active power losses and to improve the voltage profile of the system using bio-inspired optimization algorithms. Protection and Control of Modern Power Systems 2020;5(1):1–15.

[47] Mensou S, Essadki A, Nasser T, Idrissi BB. A direct power control of a DFIG based WECS during symmetrical voltage dips. Protection and Control of Modern Power Systems 2020;5(5):36–47.

[48] Mahdi B, Mehrdad A, Gevork BG, Maryam F. Short-term interaction between electric vehicles and microgrid in decentralized vehicle-to-grid control methods. Protection and Control of Modern Power Systems 2019;4(4):42–52.

[49] Wang Q, Yao W, Fang JK, Ai XM, Wen JY, Yang XB, Xie HL, Huang X. Dynamic modeling and small signal stability analysis of distributed photovoltaic grid-connected system with large scale of panel level DC optimizers. Appl Energy 2020:114132.

[50] Moharana A, Dash PK. Input-output linearization and robust sliding-mode controller for the VSC-HVDC transmission link. IEEE Trans Power Deliv 2010;25(3):1952–61.

[51] Faisal R, Badal PD, Subrata K, Sarker Sajal KD. A survey on control issues in renewable energy integration and microgrid. Protection and Control of Modern Power Systems 2019;4(4):87–113.

[52] Li JH, Wang S, Ye L, Fang JK. A coordinated dispatch method with pumped-storage and battery-storage for compensating the variation of wind power. Protection and Control of Modern Power Systems 2018;3(3):21–34.

[53] Yang B, Yu L, Zhang XS, Wang JT, Shu HC, Li SN, He TY, Yang L, Yu T. Control of superconducting magnetic energy storage systems in grid-connected micro-grids via memetic slap swarm algorithm: an optimal passive fractional-order PID approach. IET Gener, Transm Distrib 2019;13(24):5511–22.